

CRISPRED: A data pipeline for the CRISP imaging spectropolarimeter

J. de la Cruz Rodríguez^{1,2}, M.G. Löfdahl¹, P. Sütterlin¹, T. Hillberg¹, and L. Rouppe van der Voort³

¹ Institute for Solar Physics, Dept. of Astronomy, Stockholm University, Albanova University Center, 106 91 Stockholm, Sweden

² Department of Physics and Astronomy, Uppsala University, Box 516, 751 20, Uppsala, Sweden

³ Institute of Theoretical Astrophysics, University of Oslo, P.O. Box 1029 Blindern, N-0315 Oslo, Norway

Draft: 1:54pm June 10, 2022

ABSTRACT

The production of science-ready data from major solar telescopes requires expertise beyond that of the typical observer. This is a consequence of the increasing complexity of instruments and observing sequences, which require calibrations and corrections for instrumental and seeing effects that are not only difficult to measure, but are also coupled in ways that require careful analysis in the design of the correction procedures. Modern space-based telescopes have data-processing pipelines capable of routinely producing well-characterized data products. High-resolution imaging spectropolarimeters at ground-based telescopes need similar data pipelines. The purpose of this paper is to document a procedure that forms the basis of current state of the art processing of data from the CRISP imaging spectropolarimeter at the Swedish 1-m Solar Telescope (SST). By collecting, implementing, and testing a suite of computer programs, we have defined a data reduction pipeline for this instrument. This pipeline, CRISPRED, streamlines the process of making science-ready data. The pipeline is implemented and operated in IDL, with time-consuming steps delegated to C. This pipeline will be the basis also for the data pipeline of the forthcoming CHROMIS instrument.

Key words. Techniques: imaging spectroscopy — Techniques: image processing — Instrumentation: polarimeters — Instrumentation: high angular resolution

1. Introduction

State-of-the art spectropolarimeters of solar telescopes, such as the CRisp Imaging Spectropolarimeter (CRISP; Scharmer et al. 2008) of the Swedish 1-meter Solar Telescope (SST; Scharmer et al. 2003a), produce complex data sets at a high rate. The dimensions of the data sets typically include space, time, and wavelength, as well as polarization. The task of going from raw data to science ready data is beyond the skills of the majority of potential users due to the complexity of the data calibration and required compensation for seeing degradation. There is thus a strong incentive to relieve solar scientists from the burden of gaining expert knowledge about state of the art instrumentation by supplying them with easy to use data pipelines with well-characterized data products. Well-designed data pipelines allow such instrumentation to reach their full scientific potential, while minimizing the efforts of the user and opening up access to the facility to inexperienced users. Such pipelines will also be necessary in the future when solar telescopes are routinely operated in service mode and are required to deliver science-ready data to scientists (Reardon et al. 2009). The European solar community has recognized the need for such pipelines and therefore included pipeline development in the recently started EU-funded SOLARNET project.

In this paper, we describe CRISPRED¹, a data reduction pipeline for CRISP. The pipeline started as a collection of scripts written by different (present as well as former) researchers at the Institute for Solar Physics (ISP), Uppsala University, and University of Oslo, coded in a variety of languages. These hetero-

geneous pieces of code have since been incorporated into an object-oriented IDL structure with computationally demanding parts performed in C subprograms called as dynamically loadable modules (DLMs). Early versions of CRISPRED have been used by several authors to reduce and prepare their data, given that a basic framework has been functional since 2011 (e.g., Watanabe et al. 2012; Scharmer et al. 2013; de la Cruz Rodríguez et al. 2013; Vissers et al. 2013; Sekse et al. 2013; Wedemeyer et al. 2013; Rouppe van der Voort & de la Cruz Rodríguez 2013; Leenaarts et al. 2014).

A pipeline for an instrument like CRISP must be based on a detailed knowledge about the formation of the image data, including the various sources of measurement error and the calibrations that allow them to be characterized. Section 2 describes the image formation relevant for CRISP.

The calibration and removal of the errors and contaminations are important parts of the pipeline. Section 3 describes the main data processing steps included in CRISPRED. Recent developments are described in more detail in Sect. 4. We end with a discussion on future developments in Sect. 5.

2. Formation of CRISP images

The signal that can be detected by CRISP, intensity and polarization of light with a wavelength between 500 nm and 855 nm, is formed in the Sun's photosphere and chromosphere. The intensity pattern over the field of view (FOV) is modulated by the polarization optics and the final image is the convolution of this intensity pattern with the telescope PSF at the wavelength selected by the narrowband (NB) filters.

¹ <http://dubshen.astro.su.se/wiki/index.php?title=CRISPRED>

The image formation is quite complex. Turbulence in the Earth's atmosphere degrades the image quality and causes spectral cross-talk. The telescope and the optical setup introduce undesirable polarization. The filter profiles vary over the FOV and introduce other unwanted effects. The following sections describe the image formation, including an overview of the most important deviations from the ideal case.

2.1. Atmosphere and telescope

Turbulence randomly mixes air with varying temperature (and therefore refractive index), causing perturbations in the wavefront phases that vary spatially with a time scale of ms. We refer the interested reader to Fried (1965) and Roddier (1999) for mathematical descriptions of these effects. Turbulence near the telescope aperture causes global motion and blurring of the image. Similar effects at higher altitudes (~ 10 km) take the form of variations over the FOV, where the seeing causes rubber-sheet deformations of the image and blurring that varies over small scales. Scattering from aerosols can produce a diffuse component that lowers the contrast. Particularly in *calima* conditions, when the Saharan air layer, an elevated (1000–5500 m) layer of dry air and mineral dust originating from the Saharan desert, forms over large parts of the northern equatorial Atlantic (e.g., Dunion & Velden 2004). The polarizing effects from atmosphere are visible in the blue sky but are small in direct sunlight.

The SST is located on the island of La Palma, a little less than 2400 m above sea level in a 17-m high tower. Figure 1 shows the optics of the telescope. Via the two 45° turret alt-az mirrors, the beam is directed down through the vertical telescope tube to a primary focus on the bottom plate. The alt-az configuration causes image rotation and the rotation of the lens and two mirrors cause time-varying polarization (Selbing 2005), mostly far from focus. The lens itself is a singlet and therefore has enormous chromatic aberrations. These are removed by a Schupmann corrector, that is fed from a field mirror on the bottom plate of the tube and forms a new focus just outside an exit vacuum window behind a large baffle.

2.2. Pre-CRISP optics

We refer now to Fig. 2, where we show a schematic view of the optical setup below the telescope, the details of which are described in this section.

The field lens (FL) is near the focus from the Schupmann corrector and it is designed to form a 34 mm diameter pupil image at the Adaptive Optics (AO) deformable mirror (DM). Near the Schupmann focus, various artificial targets and field stops can be slid into the beam. Just outside the science FOV, a part of the beam is reflected toward a wide-field wavefront sensor (WFS – not shown in Fig. 2), that can be used for monitoring the seeing profile above the telescope (Scharmer & van Werkhoven 2010).

The AO has two parts. The correlation tracker (CT) measures image motion and uses the tip-tilt mirror (TM) to keep the image steady. The recently installed 85-microlens Shack–Hartmann WFS measures the phase of the wavefront at the pupil and tries to keep it flat by controlling the shape of the 85-electrode monomorph DM from CILAS at a rate of 2 kHz. This system (Scharmer et al., in preparation) is similar to the previous system by Scharmer et al. (2003b), although it is an upgrade in both hardware and software.

Between the target slider and the TM, polarization calibration optics (PCO) can be inserted in the beam. There are three

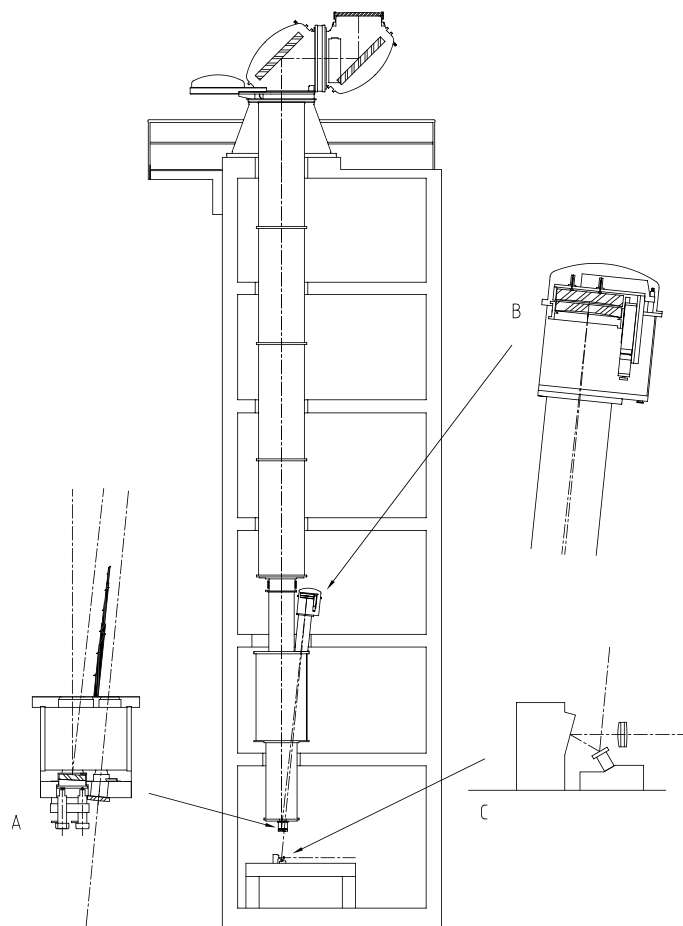


Fig. 1: Sketch of the SST, from the 1-m lens, via the two alt-az mirrors, the field mirror on the bottom plate (inset A), the Schupmann corrector (inset B), the field lens and exit window (inset A), to the tip-tilt mirror, deformable mirror, and re-imaging lens on the optical table (inset C). Optical path continues in Fig. 2. Courtesy of Göran Scharmer.

parts: a red filter, a rotatable linear polarizer, and a retarder. They are not in the beam during normal science observations.

The TM and DM together make the beam horizontal and send it through the reimaging lens (RL) toward the dichroic beamsplitter (DC), which splits the beam (at 500 nm) into a red beam and a blue beam. The CRISP is in the red beam, behind a beamsplitter that sends a small fraction of the light to the AO WFS.

2.3. CRISP

The tunable filter of the CRisp Imaging Spectropolarimeter (CRISP, Scharmer 2006; Scharmer et al. 2008) is a dual Fabry–Pérot interferometer consisting of two etalons mounted in tandem in a telecentric configuration. An etalon consists of a cavity with two reflecting plates where the light undergoes multiple reflections. An infinite train of transmission peaks is produced by multiple interference of light inside the cavity. The FPI produces quasi-monochromatic images by combining a high spectral resolution etalon (HRE) that defines the observed wavelength and a lower spectral resolution etalon (LRE) that suppresses the first few orders of secondary HRE transmission peaks. A prefilter limits the spectral range of the light that passes through the

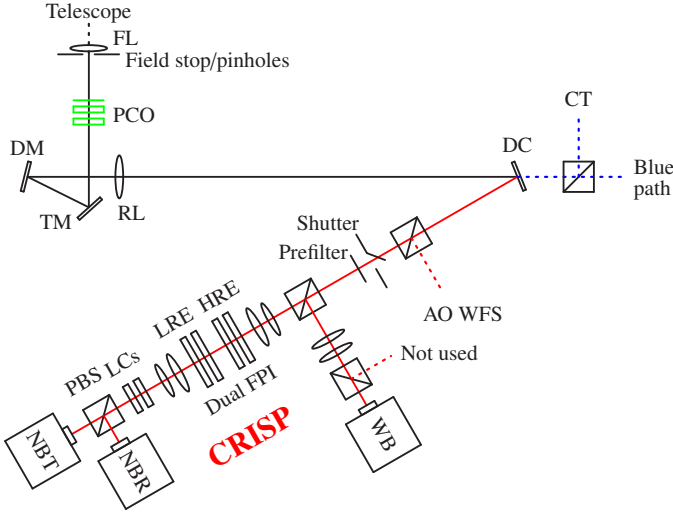


Fig. 2: Sketch of optics, from bottom of telescope (inset A in Fig. 1) to the CRISP. FL = Field Lens, PCO = Polarization Calibration Optics (not in the beam during normal observations), TM = Tip-tilt Mirror, DM = Deformable Mirror, RL = Reimaging Lens, DC = Dichroic Beamsplitter, CT = Correlation Tracker, AO WFS = Adaptive Optics WaveFront Sensor, FPI = Fabry–Pérot Interferometer, HRE = High Resolution Etalons, LRE = Low Resolution Etalons, WB = Wideband, NBT = Narrowband Transmitted, NBR = Narrowband Reflected, LCs = Liquid Crystal modulators, PBS = Polarizing Beam Splitter.

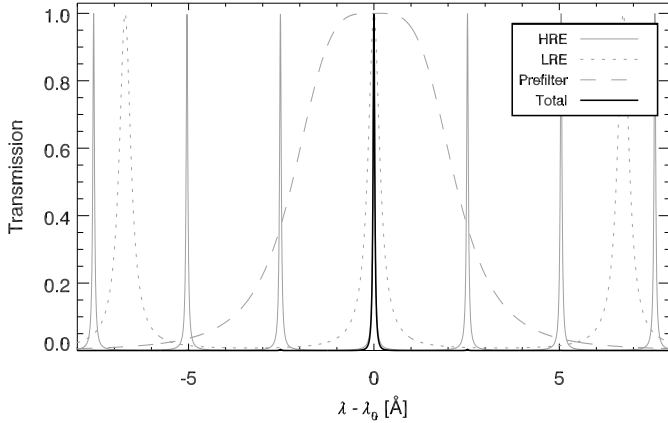


Fig. 3: Approximate CRISP transmission profile at 630 nm, computed theoretically assuming perpendicular incidence of the beam with the surface of both etalons. The individual contributions from the high-resolution etalon, the low-resolution etalon, and the prefilter are shown along with the total transmission. All curves are normalized to unity.

optical system, attenuating all higher order transmission peaks of both etalons (see Kentischer et al. 1998; Cavallini 2006; Scharmer 2006, and references therein).

Figure 3 shows the individual transmission curves for the two etalons, the prefilter and the total CRISP transmission. Note that the total transmission curve corresponds to that at the center of the prefilter. Observations in the outer flanks of the prefilter curve have larger contributions from the first few secondary transmission peaks.

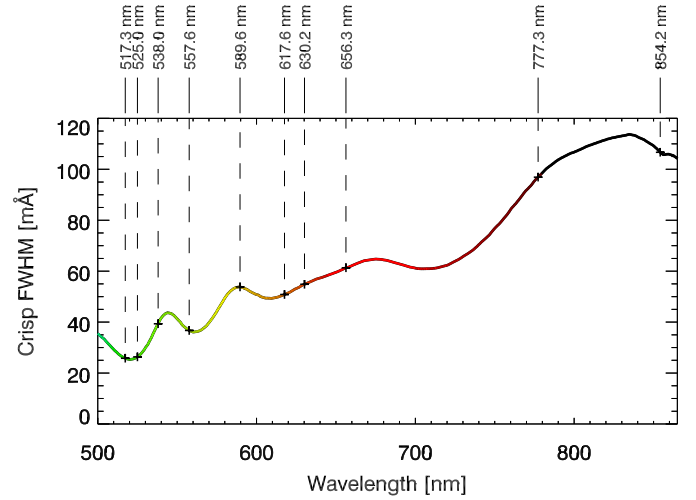


Fig. 4: Full width half maximum of the CRISP transmission profile as a function of wavelength. We have indicated those lines that are currently observable (i.e. a prefilter is available).

The transmission profile of each etalon can be approximately computed for each ray as described by Kentischer et al. (1998),

$$T(\delta\lambda, \delta R) = \frac{1}{1 + \frac{4(R + \delta R)}{(1 - R - \delta R)^2} \sin^2\left(\frac{\Psi(\delta\lambda)}{2}\right)}, \quad (1)$$

where R is the reflectivity of the etalon, and Ψ is the phase difference of succeeding reflections between the two reflecting plates:

$$\Psi(\delta\lambda) = 2 \cdot \left(\frac{2\pi}{\lambda + \delta\lambda}\right) \cdot n \cdot D \cdot \cos\theta, \quad (2)$$

where λ is the wavelength, $\delta\lambda$ is the cavity error², n is the refractive index of the cavity, D is the nominal separation between the reflecting surfaces of the etalons, and θ is the angle of incidence of the beam.

The telecentric mount was chosen because it optimizes the image quality in the focal plane (see Scharmer 2006). However, this design introduces field-dependent variations in the transmission profile:

- *Imperfections on the surface of the etalons* influence the phase difference among successive reflections between the reflecting plates of the etalons. Thus, the position of the central wavelength of the transmission profile varies over the etalon surfaces, producing field-dependent wavelength shifts of the observed spectral lines.
- *Reflectivity variations* in the coating of the etalons make the width of the transmission profile to change along the field of view.

We discuss in detail the characterization of CRISP parameters and the treatment of cavity errors in Sect. 3.2 and 4.1.

The CRISP transmission profile depends critically on the reflectivity of the coating of the etalon: narrower profiles correspond to higher values of the reflectivity. Figure 4 shows the full

² The cavity error is really an error in the cavity separation D . Attributing it to the wavelength is mathematically equivalent ($\delta\lambda = \delta D \cdot \lambda/D$) and makes it immediately useful for correction of the data.

Table 1: List of prefilters for the CRISP instrument.

CWL [nm]	FWHM [nm]	Main diagnostic	PC
517.33	0.30	Mg I	517.2
525.01	0.30	Fe I	525.0 ✓
538.20	0.34	C I	538.0 ✓
557.80	0.30	Fe I	557.6
*587.6	0.4	He I	587.6
589.70	0.39	Na I	589.6
617.39	0.42	Fe I	617.3 ✓
630.26	0.44	Fe I	630.2 ✓
656.38	0.49	H I	656.3
777.24	0.77	O I	777.2 ✓
854.16	0.93	Ca II	854.2 ✓

Notes. *Ordered from the manufacturer at the time of this publication. PC: Calibrated for polarization effects, see Sect. 3.4.

width half maximum (FWHM) of the CRISP transmission profile as a function of wavelength. To derive the FWHM, we have used the nominal reflectivity values of the etalons as measured by the manufacturer and Eq. (1).

Currently ten prefilters are available to observe selected spectral lines, which have been indicated in Fig. 4 and detailed in Table 1. Selection of the appropriate prefilter for each observing sequence is done by means of a filter wheel that is located near a focal plane (see Fig. 2). The central wavelength (CWL) of the filters are slightly to the red of the line core for which they are designed. The whole filter wheel sits on a motorized tiltable mount, which allows tuning of the filters to the exact wavelengths. In some cases this allows easy observation of other interesting spectral lines close to the primary one.

The CRISP instrument includes three cameras, one acquiring wideband (WB) images and two NB cameras. After the prefilter wheel, a beam splitter sends the light to the WB (8%) and NB channels (92%) respectively.

Reimaging optics are placed before and after the etalons to make the beam slower at the location of the etalons, and to place the focus between the two etalons. After the second re-imaging, a pair of modulators³ produce four polarization states that are linear combinations of the four Stokes parameters. Finally, a linearly polarizing beam splitter separates the light into horizontal and vertical polarized components and sends them to the respective NB camera.

2.4. Detectors

The light in the final focus is recorded by three Sarnoff CAM1M100 cameras with back-illuminated, thinned CCD detectors consisting of 1024 by 1024 $16 \times 16 \mu\text{m}^2$ pixels. At near-IR wavelengths the silicon substrate is semi-transparent, causing problems with back-scattering of light from electronics and other parts interior to the cameras (de la Cruz Rodriguez 2010).

The finite pixel area causes a slight reduction of signal at the highest detected spatial frequencies. The corresponding modulation transfer function (MTF) also includes a wavelength depen-

³ The present modulators are a pair of nematic liquid crystals that change their states too slowly to finish during the covered phase of the chopper. They are therefore operated with overdrive, making them very sensitive to temperature variations within the observing room. New, faster modulators of the type described by de Wijn et al. (2011) will be installed during the 2014 season.

dent component from charge diffusion that is more difficult to model (Stevens & Lavine 1994).

The three cameras are synchronized by use of external shutter (chopper), to facilitate image restoration. The chopper revolves at ~ 37 Hz with an exposure time of ~ 17 ms, using the covered ~ 10 ms for read out.

3. Data reduction steps

Figure 5 illustrates the data flow of the CRISPRED pipeline. All the details are provided in the following sections, but we include here a very brief summary of the data flow.

The following effects are compensated for within the pipeline. Some effects are coupled, which makes the processing more complicated.

1. Spatial variation in detector gain and zero level offset (bias), IR transparency.
2. Spatial variation in the CRISP FPI passband profiles; reflectivity, cavity errors.
3. Optical aberrations from atmospheric turbulence (seeing) as well as from the optics.
4. Inter-camera misalignments.
5. Field-dependent and time-varying instrumental polarization.
6. Image field rotation, temporal misalignment and rubber-sheet warping from seeing.

The first steps in a typical reduction are to perform the polarimetric calibration (Sect. 3.4) to derive a demodulation matrix for each pixel. The latter are used to demodulate the flat-field data. We use the Stokes I flat-field images to characterize CRISP (Sect. 3.2). We prepare our flat-field images using spectra from real observations and our processed flats (Sect. 4.1).

Our two NB cameras and the WB camera are aligned using pinhole images (Sect. 4.2), that allow the estimation of offsets in (x, y) positions. These offsets are used by the MOMFBD program in order to make restored images that are well aligned (Sect. 3.3.1).

The restored images are demodulated and compensated for telescope-induced polarization (see Sect. 3.4). Later, we estimate and apply corrections to obtain a homogeneous time-series (Sect. 3.6).

3.1. Detector effects

The pixel by pixel gain and bias are in principle easy to calibrate. Exposures collected while the beam is blocked (dark frames) establish the bias and flat fields establish the gain. The flats are collected while moving the telescope pointing in a circle over quiet Sun near disk center and blurring the image by putting out random voltages on the DM. Flats are collected individually for each wavelength tuning and polarization state.

Both darks and flats are made by averaging many (~ 1000) exposures in order to reduce shot noise and – in the case of flats – reduce the influence of solar structures. We check statistics for all dark and flat frames and remove outliers before summing. This way we essentially remove the risk of having the final flats and darks being destroyed by the occasional camera or shutter glitch, birds flying in front of the telescope aperture, etc.

Bad pixels are zeroed in the gain tables to be read by the MOMFBD program, which interprets zero gain pixels as an instruction to calculate interpolated values for the corresponding pixels in the image data. Isolated or small groups of bad pixels are found with heuristics based on identifying outliers in a

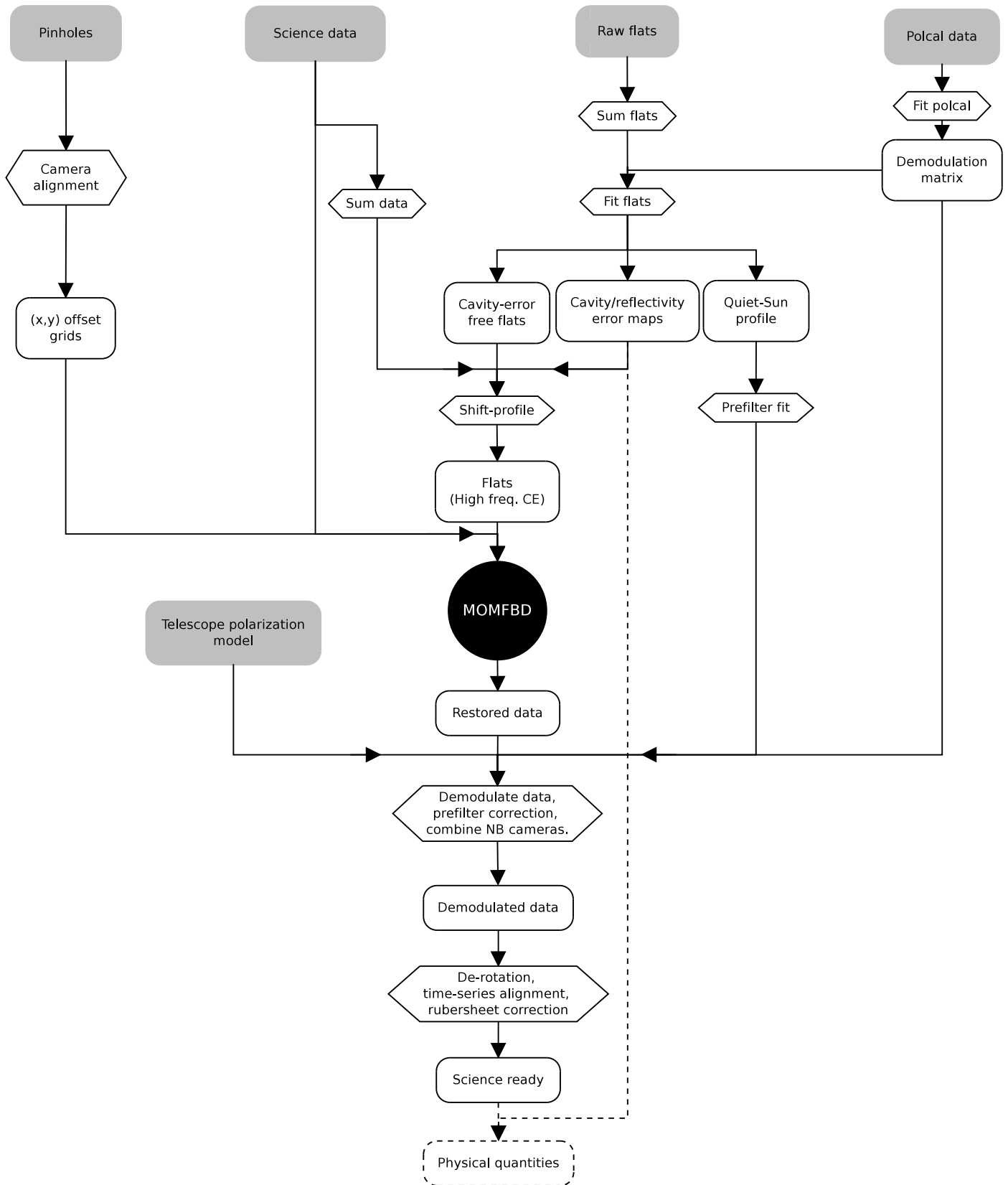


Fig. 5: Data flow in the CRISPRED pipeline. Starting points are the rounded boxes with a gray background: the raw data and the telescope polarization model. The diamond boxes indicate fitting and other processing. Products from fitting routines or data processing are represented by rounded, white boxes. The distinct symbol for the MOMFBD processing indicates that it is not done in IDL. Reflectivity and cavity errors must be included in the interpretation of the science data (outside the CRISPRED pipeline, hence indicated with dashed lines). All science and calibration images are corrected for dark current.

unsharp-masked version of the summed flat fields. The Sarnoff camera detectors are divided into 2×8 “taps”, regions that are read out separately. We have found that pixels on the border of those taps cause artifacts in the image restoration, so these pixels are routinely marked as bad. Because of this, the absolute majority of pixels to be interpolated by the MOMFBD program are oriented in columns. We have found that we get less artifacts if we choose to do 1-dimensional interpolation across those columns instead of the default circularly symmetrical interpolation.

A WB observed image is corrected by pixel-by-pixel subtraction of the bias and division with the gain. However, the flats correct not only for detector characteristics but also for imperfections in the near-focus optical elements, e.g. dust. These effects couple with polarization and are therefore time-dependent for the NB images. The procedure for dealing with this is described in Sect. 4.1 below.

An additional problem occurs at near-IR wavelengths, longer than approximately 700 nm (currently affecting data acquired with the 777 nm and 854 nm CRISP prefilters). Images collected with the Sarnoff CAM1M100 CCDs show a pattern consisting of straight lines that is not present at other wavelengths and that cannot be removed with traditional flat-fielding (with or without the polarization procedure described in Sect. 4.1). The pattern is an imprint of the electronics of the cameras, caused by the silicon substrate being semitransparent in near-IR. The back scatter can be modeled with a PSF describing the scattering in the material behind the CCD and a gain factor representing the amount of light that returns from that direction. The procedure is described by de la Cruz Rodríguez (2010) and de la Cruz Rodríguez et al. (2013, Appendix A.1).

3.2. Characterization of CRISP

The way flat-fields (flats) are made, by averaging many short-exposure images collected while the telescope moves in small circles around the center of the solar disk, allows the assumption that the spectrum present at each pixel corresponds to a spatially averaged quiet-Sun profile at disk center. Figure 6 is a snapshot of the turret software with a virtual representation of the solar disk with the active regions indicated with red labels. The blue path indicates the trajectory followed by the turret to acquire flat-field data. The presence of active regions can sometimes be inconvenient, forcing the observer to trace more elliptical trajectories. To avoid distortions in the quiet-Sun profile, we normalize the NB flats by use of the mean intensity of the WB flat images (acquired simultaneously with the NB images) as they should average to the same value for all wavelengths.

To characterize the cavity-error map, we use a self-consistent method proposed by Schnerr et al. (2011). The basic idea is to remove the imprint of spectral lines from the summed flats. The presence of cavity and reflectivity errors, fringes and variations of the prefilter across the FOV, can be understood as a distortion of the profiles, and it can be modeled using a self-consistent iterative scheme, here implemented in an external multi-threaded C++ module that makes use of a Levenberg–Marquardt algorithm to fit the data (cMPFIT, Markwardt 2009).

In the first iteration, cavity errors are unknown, so we estimate the quiet-Sun profile by fitting a cubic non-overshooting Bezier-spline (Auer 2003) to the average spectrum in the flats. That average spectrum is shifted in wavelength and scaled in intensity to match the observed spectrum at each pixel, providing a first estimate of the cavity-error map and the gain at each pixel. For stability purposes, in this first iteration, the reflectivity and prefilter variations are assumed to be constant.

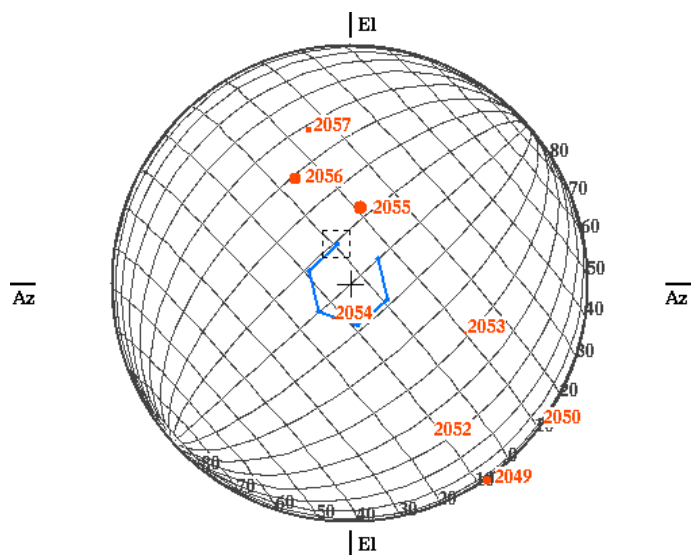


Fig. 6: Snapshot from the turret software, where active regions are indicated with red labels over a theoretical representation of the solar disk. The blue path represents the trajectory that is repeatedly followed by the telescope during the acquisition of flat-field data.

Using the fitted values, we place all spectra (across the field of view) in a large array of (λ, I) values, corrected for the cavity error shift and gain value. A new estimate of the quiet-Sun average is derived by fitting a Bezier-spline to all data points. In the following iterations, a slightly more complete model is used to fit the data, including the gain value, a cavity-error, reflectivity fluctuations and prefilter/fringe variations. The latter are fitted using a polynomial multiplicative term to the average spectrum. The model is summarized as follows:

$$I(\lambda) = G \cdot \mathfrak{F}^{-1} \left\{ \mathfrak{F} \{ \hat{I}(\lambda) \} \frac{\mathfrak{F} \{ T(\delta\lambda, \delta R) \}}{\mathfrak{F} \{ T(0, 0) \}} \right\} \left(1 + \sum_{n=1}^N c_n \lambda^n \right), \quad (3)$$

where G is the value of the gain, \hat{I} is the estimate of the quiet-Sun average, $T(\delta\lambda, \delta R)$ is the CRISP transmission profile at a given pixel (defined in Eq. (1)), $\delta\lambda$ and δR are the cavity and reflectivity errors respectively, and c_n are the coefficients of the multiplicative polynomial component. Note that $T(0, 0)$ is a CRISP transmission profile computed using the reflectivity value provided by the manufacturer and no shift. Also note that the length of the polynomial component can be adapted to each case, depending on the wavelength coverage of the observations and how strong fringes are at that wavelength. The \mathfrak{F} operator represents the one-dimensional Fourier transform and \mathfrak{F}^{-1} its inverse. At each pixel, we fit the value of $\delta\lambda$, δR and c_1, \dots, c_n . Further details are given by Schnerr et al. (2011).

Figure 7 illustrates the resulting reflectivity (top) and cavity (middle) error maps that are inferred using our routines. In the bottom panel we represent a two-dimensional histogram computed from all spectra in the FOV, corrected for cavity errors, normalized by the gain value and corrected for the polynomial component. In this figure we have not corrected the data for reflectivity errors, although those are included in our model. Once all the corrections are applied, we expect all data points to tightly describe the same spectral profile.

Chromospheric lines, like H I $\lambda 6563$ and Ca II $\lambda 8542$, are significantly wider than the CRISP transmission profile. Under

those circumstances, if the slope of the line has a linear behavior within the width of the transmission profile, the imprint of reflectivity variations is extremely mild and this approach fails most of the times, especially when the observations are not critically sampled in the spectral dimension. Instead, the inferred reflectivities are usually dominated by a fringe pattern.

Therefore, a simplification to this scheme was proposed by de la Cruz Rodríguez et al. (2013), where reflectivities are assumed to be constant across the field of view and the model can be simplified enormously as convolutions become unnecessary and the mean spectrum can be shifted using cubic Bezier interpolation.

3.3. Image restoration

3.3.1. MOMFBD

Images are restored from wavefront aberrations by means of the Multi-Object Multi-Frame Blind Deconvolution (MOMFBD; van Noort et al. 2005) method, based on the algorithm by Löfdahl (2002). Not using any assumptions about the aberration statistics, the method can compensate for optical aberrations, both from the atmosphere and from the optics, and partial compensation by the AO does not introduce any extra complexity. However, we do take the aberration statistics into account by using atmospheric Karhunen–Loève modes (KL, Roddier 1990) in the expansion of the pupil phase. These modes are constructed so they are both orthogonal on a circular aperture and statistically uncorrelated assuming atmospheric turbulence following a Kolmogorov model.

The correction is limited by the finite parametrization of the wavefront, so high-order aberrations from both sources are not corrected. The uncorrected aberrations show up in the restored data as a stray light component. By default, we are currently using the 35 most significant atmospheric KL modes as basis functions for expanding the unknown wavefronts. This number was set to about the same as the number of modes corrected by the AO. However, as the AO was recently upgraded to correcting 85 modes, the default number of KL modes routinely used in MOMFBD will probably be increased.

The MOMFBD algorithm is based on the assumption that the aberrations are isoplanatic, so that the point spread function (PSF) is constant within the FOV. This makes it possible to find the PSF and deconvolve the raw data by use of fast Fourier transforms. In the process, each subfield is low-pass filtered individually based on the local signal-to-noise ratio (SNR). In order to make this assumption hold, at least approximately, the processing is done on overlapping subfields of a ~ 5 arcseconds squared. The restored subfields are then mosaicked, resulting in a restored version of the entire FOV.

3.3.2. Alignment

Physical quantities like Stokes maps and Dopplergrams are calculated as linear combinations of intensity images from different modulator states or wavelength tunings (here: just *states*). The physical quantities are encoded as small variations in the intensity. If the images involved are not properly aligned, there will be artifacts in the calculated quantities. However, because the intensity structures differ from state to state, cross correlation methods are not useful for alignment of images from different states.

Given accurate information about the alignment of cameras from the pinhole array (see Sect. 4.2), the MOMFBD joint pro-

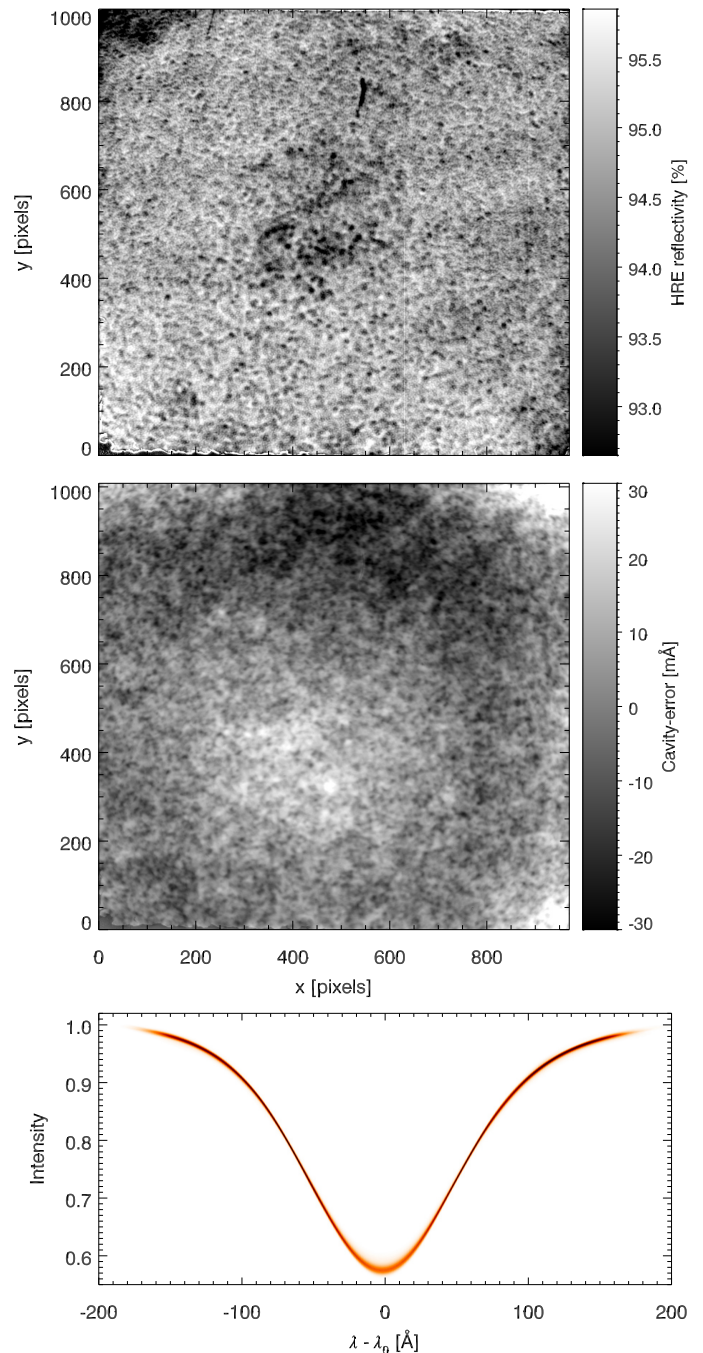


Fig. 7: Characterization of the CRISP instrument at 617 nm. *Top*: Reflectivity fluctuations of the high resolution etalon. *Middle*: Cavity error map. *Bottom*: two-dimensional histogram of the quiet-Sun spectra from the flat field, where each spectrum (from a different pixel) has been shifted to correct the cavity error and scaled according to the gain value.

cessing of images from the WB camera with the variable states images from two NB cameras will make all the restored images from a single scan aligned to subpixel precision (van Noort et al. 2005). The reason this works is that all the WB images go into making a single restored image (the *anchor* image), forcing the estimated wavefronts (mainly the tip and tilt components) to be such that they align the raw WB images. Every NB image is si-

multaneous to one of the WB images, and their estimated wavefronts are constrained to differ by exactly the fixed tip and tilt offset that align the cameras.

In spite of the subfielding, there are residual anisoplanatic effects in the restored data. Because the raw images for the different NB states are not collected simultaneously, these residuals vary from state to state. This results in relative geometric distortions on scales smaller than the subfields. In the CRISPRED pipeline, we have implemented the improvement suggested by Henriques (2012), capable of removing also such differential stretching from the restored NB images: In addition to the restored WB image based on the entire sequence of raw WB images, the MOMFBD program makes a set of additional restored WB images, each based on only the raw images corresponding to the raw NB images of each state. We then calculate alignment parameters (stretch vectors) on a grid, that align this WB image with the anchor WB image, and apply them to the corresponding restored NB image. Note that this does not remove the variable blurring at scales smaller than the subfields.

3.3.3. Post-restoration low-pass filtering

We have implemented an optional procedure for low-pass filtering restored image sets. The main motivation for such procedures is that physical quantities are often calculated by differential combination of images (e.g., magnetograms and Dopplergrams). In general they would be low-pass filtered differently by MOMFBD (depending on their individual SNR), which means that there are spatial frequencies in which one image has signal where the other does not. In addition, MOMFBD low-pass filters the subfields but the act of mosaicking them adds new noise at mid to high spatial frequencies. Therefore we want to filter all images in such a set with a common filter.

The idea is to analyze the power spectrum of each image in a set and construct a low-pass filter that matches its signal dominated area. The common filter is then constructed by selecting the minimum value of all filters at each spatial frequency point individually. See Löfdahl et al. (2011) for an example (although not with CRISP data).

In theory, there should be an easily identifiable drop in power from the low-frequency, signal-dominated part of the Fourier domain to the high-frequency part that is noise dominated in the raw data and zeroed by noise filtering as part of the image restoration procedure. However, in our experience this is not always so. We have implemented several different algorithms that can be used depending on the data at hand. This is by necessity an interactive step.

3.4. Polarimetric calibration

Above the position of the PCO, the SST contains three lenses and four mirrors that modify the polarization properties of the light. Additionally, the optical table where the CRISP instrument is mounted contains a train of optical elements that also affect polarization (see Fig. 2). We use two modulators to produce four polarization states that are linear combinations of the wanted Stokes parameters. A linearly polarizing beam splitter is used to split the beam in two orthogonal states that are detected simultaneously by each of the NB cameras. This dual-beam setup is necessary for removing, to first order, seeing-induced polarization cross-talk (see Casini et al. 2012, and references therein). For each camera and wavelength, and in each (x, y) pixel, the

intensity for the four polarization states can be written as

$$\mathbf{I}_{\text{obs}}(x, y) = \mathbf{M}_{\text{table}}(x, y) \mathbf{M}_{\text{tel}}(\theta, \varphi) \mathbf{I}_{\text{real}}(x, y), \quad (4)$$

where \mathbf{I}_{obs} is the detected intensity vector, \mathbf{M}_{tel} is the telescope matrix (which depends on the azimuth φ and the elevation θ of the telescope pointing) and $\mathbf{M}_{\text{table}}$ is the modulation matrix and \mathbf{I}_{real} is the real Stokes vector (I, Q, U, V) . Selbing (2005) proposed a telescope polarization model for the SST and provided a telescope matrix \mathbf{M}_{tel} for 630 nm. We use a similar model and up-to-date parameters have been acquired for the prefilters relevant for polarimetry as indicated in Table 1.

The SST polarization model is constructed using the Mueller matrices of each polarizing element,

$$\begin{aligned} \mathbf{M}_{\text{tel}}(\theta, \varphi) = & \mathbf{R}_{f+}(a_{11}) \cdot \mathbf{N}_s(a_9, a_{10}) \cdot \mathbf{N}_f(a_7, a_8) \\ & \cdot \mathbf{R}_{f-}(a_{11}) \cdot \mathbf{R}_{\text{az}}(\varphi) \cdot \mathbf{N}_{\text{az}}(a_5, a_6) \cdot \mathbf{R}_{\text{el}}(\theta) \\ & \cdot \mathbf{N}_{\text{el}}(a_5, a_6) \cdot \mathbf{L}(a_0, a_1, a_2, a_3, a_4). \end{aligned} \quad (5)$$

In this model, the entrance lens (\mathbf{L}) is a composite of retarders that modulate the light (5 free parameters). Mirrors are noted with \mathbf{N} and have two free parameters. Rotations to a new coordinate frame are indicated with \mathbf{R} . The exact form of these matrices is given by Selbing (2005). The properties of the optical elements are wavelength dependent and are contained in the model parameters a_0, a_1, \dots, a_{11} .

The polarimetric calibration of the optical table is performed as described by van Noort & Rouppe van der Voort (2008), summarized here for completeness. To acquire the calibration data, known polarization states are generated using a linear polarizer and a quarter-wave plate (QWP hereafter), located just after the exit window of the telescope (PCO in Fig. 2). Typically, for each linear-polarizer angle, the QWP rotates 360° in 10° steps. Two linear-polarizer angles suffice to accurately infer the modulation matrix $\mathbf{M}_{\text{table}}$. The presence of polarizing optics close to some of the focal planes introduces significant field-dependent fluctuations in the elements of the matrix. To account for them, the elements of $\mathbf{M}_{\text{table}}$ are estimated (fitted) for each pixel on the CCD using a multi-threaded C module.

After the MOMFBD process, blurred versions of the demodulation matrix (the inverse of the modulation matrix $\mathbf{M}_{\text{table}}$) is applied to the restored images on a pixel by pixel basis as described by Schnerr et al. (2011). Basically, for each NB camera, the demodulation matrix is clipped in the same subfields as the images, then convolved with the average seeing PSF of the corresponding patch and, finally, stitched together in the same way as the restored images. Before applying the demodulation matrix to the data, residual seeing distortions are removed from each of the polarization states as described by Henriques (2012).

Data from the two NB cameras are combined after demodulation and normalization with respect to the mean intensity (Stokes I), so each contribute with the same weight to the average. This step is necessary because the cameras do not have strictly the same gain.

Telescope polarization is compensated for in a subsequent step, if the parameters of the telescope model are known for the observed spectral region.

3.5. Prefilter correction

In Sect. 3.2 we estimate the spatially averaged quiet-Sun profile from the flat-field data. Similarly to Schnerr et al. (2011), we degrade the FTS solar atlas (Braut & Neckel 1987) with a theoretical CRISP profile and a theoretical prefilter curve to reproduce our observed quiet-Sun profile.

We adopt a Lorentzian profile to describe the prefilter, with the following parameters:

$$P(\lambda; p_1, p_2, p_3, p_4, p_5) = \frac{p_1}{1 + \left(2 \cdot \frac{\lambda - p_2}{p_3}\right)^{2p_4}} \cdot (1 + \lambda \cdot p_5), \quad (6)$$

where λ is the wavelength offset from line center, p_1 is a scaling factor, p_2 is the central wavelength of the prefilter relative to line center, p_3 is the full width half maximum of the prefilter, p_4 is the number of cavities of the prefilter (normally fixed to 2) and p_5 is a term to account for asymmetries in the prefilter curve. Our implementation allows to fix the value of some parameters, which can be useful if the number of observed line positions is small or restricted to a small wavelength range.

The estimated prefilter curve is used to compensate the science data.

3.6. Post-processing of time-series

Once the data are reconstructed with MOMFBD and the polarimetric calibration has been applied, we compute time dependent corrections to obtain a homogeneous time series using the WB images. In a second step, we apply those corrections to the NB images to create science-ready data cubes. Polarimetric data sets result in sequential cubes with shape $n_x \times n_y \times n_\lambda \times n_{\text{Stokes}} \times n_t$, whereas non-polarimetric data have one dimension less, $n_x \times n_y \times n_\lambda \times n_t$. Our output is compatible with CRISPEX⁴, a versatile tool for the exploration of multi-dimensional data sets by [Vissers & Rouppe van der Voort \(2012\)](#).

Image field rotation angles are computed theoretically from the position of the Sun on the sky and a telescope pointing model. After de-rotation, the WB images are co-aligned using cross-correlation methods. The residual rubber-sheet motions that usually appear among the different time steps, are removed by resampling following [Shine et al. \(1994\)](#). In short, the idea is to divide the images in small subfields and compute the shift that aligns each subfield with a reference. These corrections are also applied to the cavity map, resulting in a different wavelength correction for each time-step.

Variations in the intensities are expected as the elevation of the Sun changes on the sky. We compute variations in the mean WB intensity during the sequence and compensate for them. The data set is also corrected for the prefilter curve that we measured in Sect. 3.5.

4. Recent developments

4.1. Flat-fielding and cavity errors

Image reconstruction techniques typically rely on processing a burst of short exposure images, where the surface of the Sun has not evolved noticeably. Under normal observing conditions, all intensity variations between the images of the burst should be produced by atmospheric distortion, if the images are monochromatic.

The CRISP instrument is mounted in telecentric configuration, close to one of the focal planes. This setup optimizes image quality, compared to the alternative collimated configuration. The disadvantage is the appearance of *random* small-scale wavelength shifts, produced by the corrugation of the surfaces and coatings of the etalons (cavity-errors hereafter).

⁴ Now included in Solarsoft and available on the web at <http://folk.uio.no/gregal/crispex/>.

The combined effect of cavity-errors and a line profile introduces in the images a pattern of intensity fluctuations partly from wavelength shifts of the transmission profile. The imprint of this pattern is strong enough to affect the wavefront-sensing process, particularly in bad seeing.

[Schnerr et al. \(2011\)](#) proposed an approximate solution: once the cavity-error map is known, one can use the quiet-Sun average profile, present in our flats, to approximately correct the effects of cavity-errors, assuming that the slope of the resolved pixel-to-pixel profile is somewhat similar to that from the quiet-Sun average. This approach allowed to easily compute a correction that makes the image smoother for the image restoration process. Afterward, the restored images would be multiplied by the ratio between this incorrect flat-field and the cavity-error free one (where the quiet-Sun profile is removed).

Obviously, there are limitations in this approach. A spectrum from a sunspot is hardly similar to a quiet-Sun mean profile, in strength, width and shape. But this approximation seems to work well when the seeing conditions are excellent, probably because the contrast of the images dominates over the intensity fluctuations introduced by cavity errors. Normally, the effect of cavity errors is stronger at *shorter* wavelengths, because the ratio D/λ in Eq. 2 is *larger*.

In Fig. 8 we illustrate a dataset acquired in the Mg I 5173 line, where the flat-fielding scheme proposed by [Schnerr et al. \(2011\)](#) leads to small-scale artifacts in some reconstructed images (left column), especially close to line center where the line profile is very steep (panel *b* and the Dopplergram in panel *a*). Note that artifacts will preferentially appear in the presence of a steep line profile and low image contrast. Those conditions may not be satisfied in all line positions (panels *c* and *d*) or even within the entire line scan.

In this study, we present a more accurate way to deal with the flat-fielding of non-monochromatic images for image restoration. The idea is to use non-reconstructed data to measure the observed spectra across the field-of-view, and then calculate the corrections needed to compensate intensity fluctuations introduced by the cavity error. For each line scan, we add all the images acquired in a burst for each wavelength, resulting in a data-cube with the structure (λ, x, y) .

Given that we have already estimated the cavity map as described in [Schnerr et al. \(2011\)](#) and [de la Cruz Rodríguez et al. \(2013\)](#), the profile at each pixel can be shifted accordingly. The flat-field that will be used to perform the image processing (F_{corr}) can be constructed using the cavity-error free flat (F_{cef}) multiplied by the ratio between the shifted and unshifted profiles:

$$F_{\text{corr}}(\lambda, x, y) = F_{\text{cef}}(\lambda, x, y) \frac{I(\lambda, x, y)}{I^*(\lambda - \delta\lambda_{x,y}, x, y)}, \quad (7)$$

where $I(\lambda, x, y)$ is the observed line profile, $I^*(\lambda - \delta\lambda_{x,y}, x, y)$ is the shifted line profile and $\delta\lambda_{x,y}$ is the cavity error at pixel (x, y) . This method should provide cavity-error free images, given that this method effectively shifts the observed line profile. In our tests, however, we noticed that some residual distortion could be introduced in the restored images because the spectra from our summed (unprocessed) data are not free of atmospheric distortions.

To overcome this inconvenience, a mathematical trick can be used ([Scharmer 2014](#), private communication). Figure 9 illustrates the cavity error map, which has been decomposed into two components: the low spatial frequencies (9.16 mÅ amplitude RMS contrast) and the high spatial frequencies (5.07 mÅ amplitude RMS contrast). Both panels are scaled between $\Delta\lambda =$

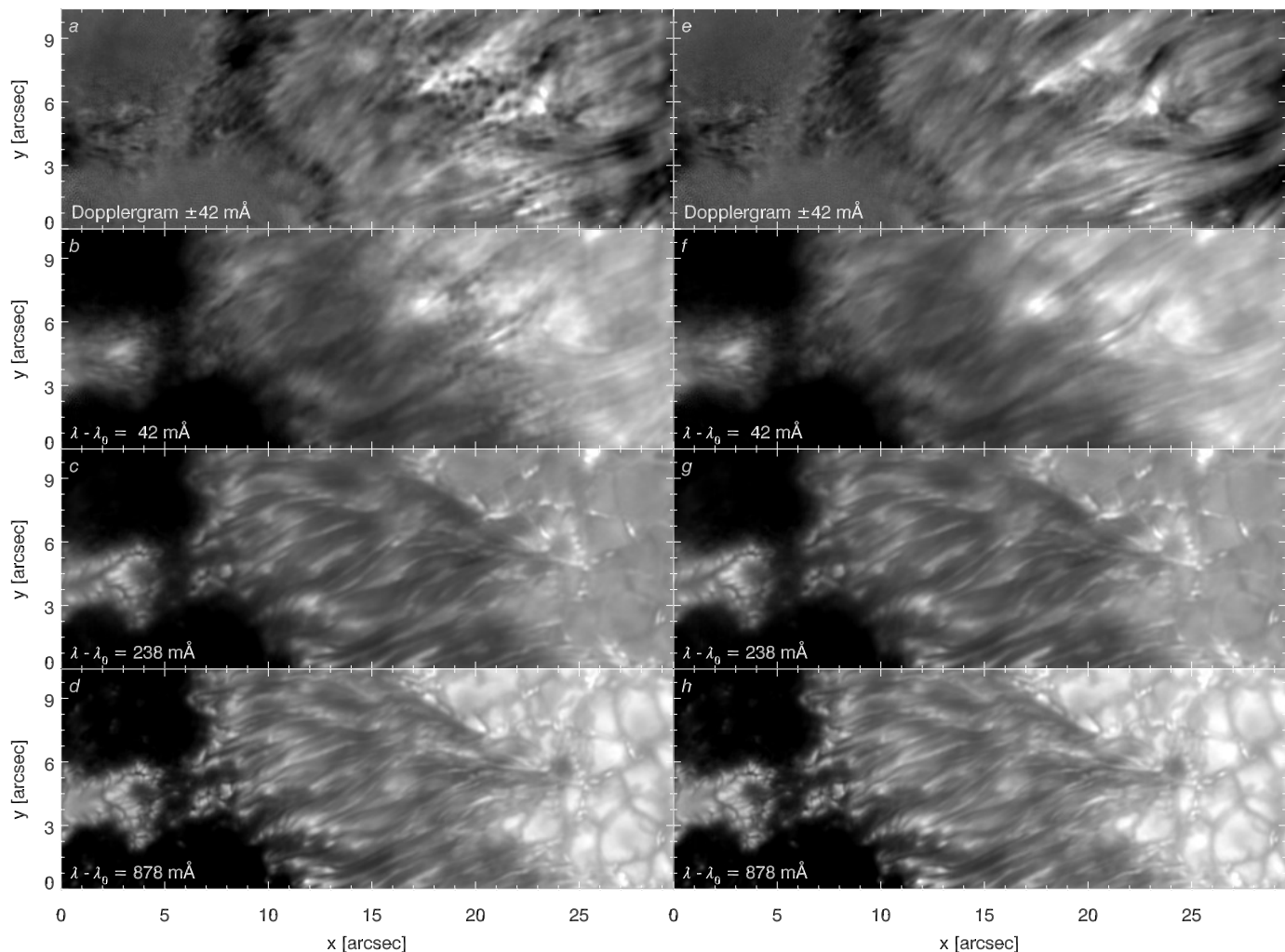


Fig. 8: Observations in the Mg I $\lambda 5173$ line. The top row corresponds to Dopplergrams (calculated from images at ± 42 mÅ). The other panels, in descending order, show red wing images, $\lambda - \lambda_0 = 42, 238,$ and 878 mÅ, respectively. The images in the left column were restored with the flat-fielding scheme by Schnerr et al. (2011). Artifacts due to cavity errors appear as small-scale grains, clearly visible in panels *a* and *b*. In contrast, no such errors are visible in the right column, corresponding to images restored with our new method.

± 30 mÅ. Note the much smaller amplitude of the high frequency component.

Due to the limited spatial extent (a few arcsec) of the PSF, the image reconstruction is only affected by the presence of high-spatial-frequency fluctuations, whereas it is rather insensitive to the presence of large scale variations. This strongly limits the distance over which intensity information from different wavelengths are mixed. Thus, it is the small-scale fluctuations that cause artifacts in the deconvolution because they are *discontinuous* to a certain extent, whereas the large-scale fluctuations do not introduce this problem.

By correcting only the high frequency fluctuations, the profile is shifted by a significantly smaller amount and potential residual distortions remain invisible. The low frequency component can be corrected after the image reconstruction, once the images are free of distortion. Also, the correction proposed in Eq. (7) is strictly more appropriate since we are assuming that the slope of the line profile at any given wavelength has linear dependence. This assumption becomes less accurate when cavity-errors are large.

We show the results of a reconstruction performed with our new method in the right column of Fig. 8. The Dopplergram and all images are free of artifacts induced by cavity errors.

4.2. Pinhole calibration

As reference for inter-camera alignment, we use a pinhole array that is mounted at the Schupmann focus. Images of this array (see sample image in Fig. 10) are routinely collected every observing day. A grid of about 12×12 pinholes fit in the detector FOV, see Fig. 10. Removing the pinholes closest to the edges leaves about 10×10 pinholes for further processing.

The maximum intensities of the pinholes are first used for finding out the relative orientation (rotation and mirroring) of the cameras, as well as alignment errors on the order of the grid spacing or larger (which should never happen). This works because the amount of light passing through the different holes depends on size and blockage by dust or dirt, forming a distinct pattern.

With pinholes rather than solar images, the object is the same in all cameras and states. By individually MOMFBD-processing

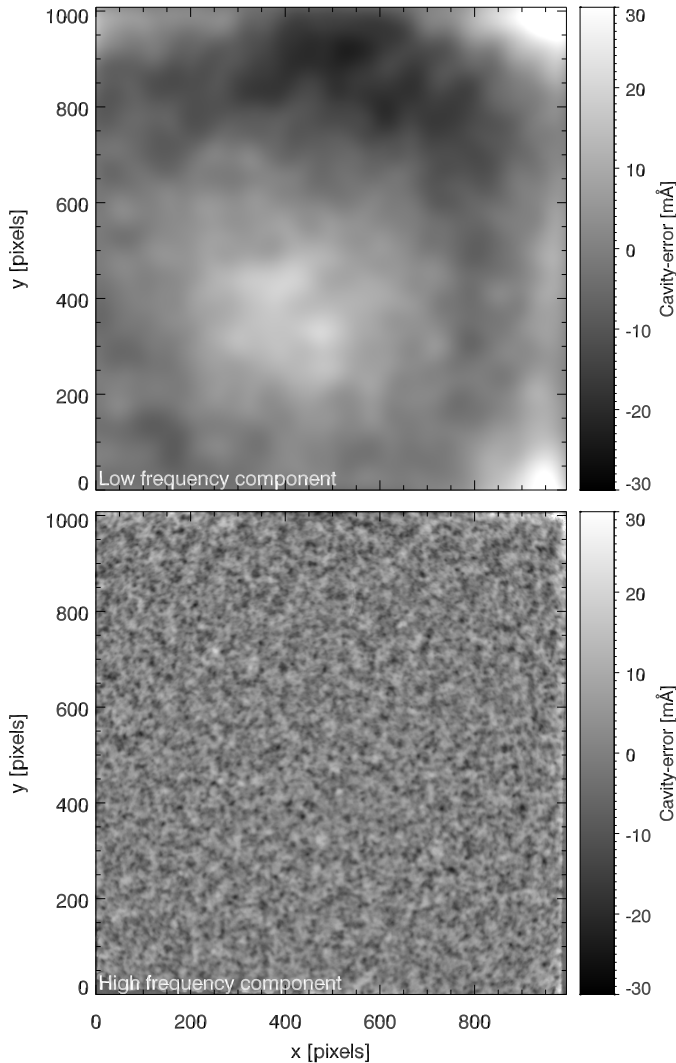


Fig. 9: The cavity error map from Fig. 7, decomposed into low spatial frequencies (top) and high spatial frequencies (bottom).

subfields centered on each of the pinholes, we estimate field-dependent alignment parameters that represent the alignment as a function of position in the FOV. Two-dimensional fits to these estimated values are stored to disk, where the MOMFBD program can look up the shifts needed to align the cameras at a particular location.

Over the last 10 years, the non-MOMFBD parts of this procedure have been implemented in ANA, shell script, python, and C++. When we re-wrote it in IDL, we also upgraded the procedure slightly.

Some pinholes are completely or partially blocked, giving bad MOMFBD inversions, see gaps in the pinhole grid in Fig. 10. Therefore we process only pinholes brighter than a threshold, reducing the number of outliers included in the fit.

Two problems with the pinhole processing were solved by methods resembling what was done by Löfdahl & Scharmer (2012), who were able to measure not only focus but also higher order aberrations from pinhole data. We now sum the pinholes with sub-pixel alignment after filling in bad pixels with interpolation. This solves the problem with sub-pixel jitter between exposures, which can violate the assumption of a common object if the sums do not involve the same exposures for all cam-

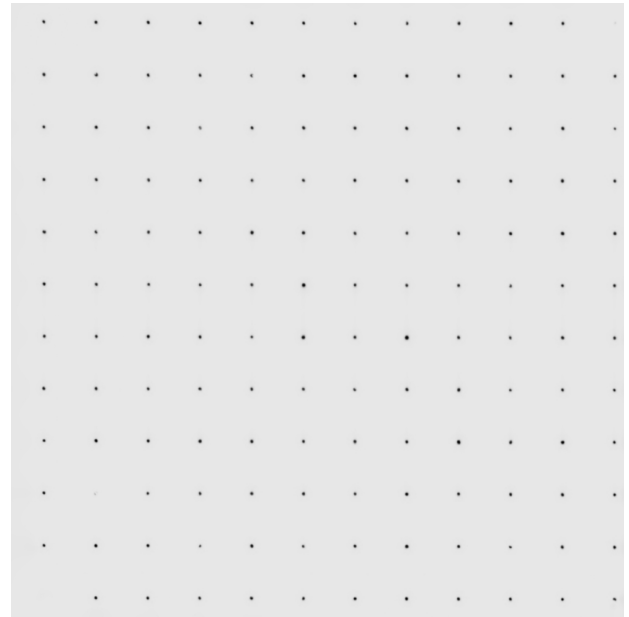


Fig. 10: A 1024×1024-pixel (60′.4×60′.4) image of the pinhole array, inverse intensity scale.

eras. We then refine the dark level of each subfield individually. When all the energy in an image is concentrated to a few pixels, also small errors in the dark level can make problems for the assumption of a common object. Using the WB as the *anchor* channel, in the old procedure, pinhole MOMFBD was run separately for WB+NBT and WB+NBR, respectively. Now we run WB+NBT+NBR, resulting in (at least potentially) more constrained inversions.

These changes improved the consistency of the estimated offset surfaces between different states. This strengthened the case for another change in the procedure. Earlier, we have mostly measured the NB pinhole shifts with respect to the WB, not only for each NB camera, but for each combination of camera, prefilter, wavelength tuning, and modulator state. This requires very large amounts of pinhole data to be collected for observing sequences with many wavelength points. The pipeline will still perform the pinhole calibration for all data that are collected but the recommendation is now to collect data only for a single state in each scan (prefilter), and then use the measured offsets for all states. An exception will be made for the very broadest lines, where data should be collected for a few wavelength tunings and the offsets then interpolated.

4.3. Image scale

Changes on the optical table can change the image scale significantly. We also discovered recently that the CRISP prefilters have a slight optical power, enough to move the focus by a few mm (optionally compensated for when observing with an extra focus term on the DM) and also change the image scale slightly. The pinhole array mounted at the Shupmann focus, used as a reference for camera alignment (see Fig. 10), is therefore used as the reference also for determining the image scale.

In order to serve as a reference, the pinhole grid spacing must be known in angular units. By use of a code developed by Norén (2013) we measured the image scale in the CRISP WB camera by comparison with approximately co-temporal 617 nm continuum images from SDO/HMI (Schou et al. 2012). Images

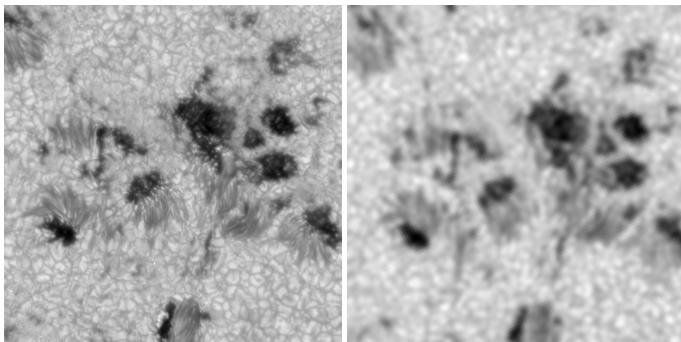


Fig. 11: Co-temporal and co-spatial 558 nm SST/CRISP (left) and 617 nm SDO/HMI (right) images used for image scale measurements. The FOV covers part of AR1589, which was near disk center on 2012-10-15.

of AR1589, an active region with many high-contrast features distributed over the SST FOV, were collected on 2012-10-15 and MFBD-restored in groups of ~ 100 exposures (sample images are shown in Fig. 11), then down-sampled to the same resolution as the HMI image. We measured in two wavelengths, through the 558 and 630 nm CRISP prefilters, and got image scales $0''.05900/\text{pixel}$ and $0''.05876/\text{pixel}$, respectively. The accuracy of these measurements is determined by two factors. The HMI image scale is known to a relative error of 0.07% or better, mostly limited by the value adopted for the solar radius (Schou 2013). The standard deviations of the image scale measurements performed separately on about 150 SST images is on the same order of magnitude, resulting in a combined uncertainty of about 0.1%.

As part of the CRISPRED pipeline, we measure the pinhole spacing (in pixels) by measuring the individual positions of each pinhole in the FOV and fitting (using MPFIT) those positions to a model with five parameters: the coordinates of the pinhole nearest the origin, the grid spacing in the two grid axis directions, and a rotation angle. Assuming we can measure the pinhole positions to better than pixel accuracy, over the ~ 1000 pixel detector size we should get accuracy that is significantly better than the 0.1% of the SST/HMI image scale calibration.

Measuring the pinhole grid spacing in pixels in pinhole array images, collected with the same cameras and on the same day as the active region data above, gives 86.75 pixels and 87.04 pixels, respectively, in the two wavelengths. This means that the measurements agree on a grid spacing of $5''.12$ ($5''.116 \pm 0''.005$) for both wavelengths. This number is used in the pipeline as the reference for calculating the image scale in all cameras. The so calibrated image scale is then used by the MOMFBD program.

5. Discussion

We have developed an object-oriented framework to reduce CRISP data sets. However, routines that are specific to other instruments can be easily incorporated in the future, i.e., the forthcoming CHROMIS instrument, a Fabry-Pérot interferometer to observe the Ca II H ($\lambda 3934$) and K ($\lambda 3968$) lines. Note that many of the routines included in this framework are also useful as building blocks for building one-shot scripts for unusual data sets.

This framework is constructed using existing routines and detailed knowledge of the instrument, to produce science-ready data sets from the raw images. We present a new approach to

compensate for the effect of cavity-errors prior to image reconstruction. This method is more accurate and, fundamentally more correct than the approximation presented in Schnerr et al. (2011), and we advise to always use it to process data from FPI instruments that are mounted in telecentric setup. Also, we have improved the existing method to co-align cameras based on pinhole images and we have implemented image-scale determination based on SDO/HMI images.

The transmission profiles of the FPI etalons were computed (see Sect. 2.3) assuming perpendicular incidence of the light. In reality, the beam is slowly converging and the low-resolution etalon is tilted to reduce ghost images. Both the tilt angle and the extreme angles from the beam convergence are $\arctan(1/165) \approx 0^\circ 17'$. These two effects in practice make the total CRISP profile slightly wider and slightly asymmetric. For simplicity, we have adopted this simplified description Eq. (1), but we plan to investigate those effects in the future and include compensation for them in the pipeline if necessary.

Some known effects are currently not included in the pipeline. Compensation for the geometric part of the detector MTF would not be difficult to add but the wavelength-dependent charge-diffusion effect requires either careful calibrations or information from the manufacturer that we do not have. There is ongoing work for the characterization of the various sources of straylight at the SST and removing their effects (Scharmer et al. 2010; Löfdahl & Scharmer 2012). When we have a good enough model for this, a correction may be added to the pipeline.

As part of the SOLARNET project, there is an effort to prepare for the inclusion of data from ground-based telescopes in a virtual solar observatory, similar to what is done for data from space-based solar telescopes. Recommendations for file formats and meta data are expected in the fall of 2014 and we aim to make CRISPRED compliant as soon as possible.

Acknowledgements. We thank Prof. G. Scharmer and Dr. D. Kiselman for illuminating discussions. The Swedish 1-m Solar Telescope is operated on the island of La Palma by the Institute for Solar Physics in the Spanish Observatorio del Roque de los Muchachos of the Instituto de Astrofísica de Canarias. This work was carried out as a part of the SOLARNET project, funded by the European Commission's 7th Framework Programme under grant agreement no. 312495. We use subroutines from the IDL astronomy User's Library (Landsman 1993). IDL[®] is a trademark of Exelis Inc. This research has made use of NASA's Astrophysics Data System (ADS).

References

- Auer, L. 2003, in ASP Conf. Ser., Vol. 288, Stellar Atmosphere Modeling, ed. I. Hubeny, D. Mihalas, & K. Werner, 3
- Brault, J. W. & Neckel, H. 1987, Spectral Atlas of Solar Absolute Disk-averaged and Disk-Center Intensity from 3290 to 12510 Å, <ftp://ftp.hs.uni-hamburg.de/pub/outgoing/FTS-Atlas/>
- Casini, R., de Wijn, A. G., & Judge, P. G. 2012, *ApJ*, 757, 45
- Cavallini, F. 2006, *Sol. Phys.*, 236, 415
- de la Cruz Rodríguez, J. 2010, PhD thesis, Stockholm University, <http://urn.kb.se/resolve?urn=urn:nbn:se:su:diva-43646>
- de la Cruz Rodríguez, J., Rouppe van der Voort, L., Socas-Navarro, H., & van Noort, M. 2013, *A&A*, 556, A115
- de Wijn, A. G., Tomczyk, S., Casini, R., & Nelson, P. G. 2011, in *Astronomical Society of the Pacific Conference Series*, Vol. 437, Solar Polarization 6, ed. J. R. Kuhn, D. M. Harrington, H. Lin, S. V. Berdyugina, J. Trujillo-Bueno, S. L. Keil, & T. Rimmele, 413
- Union, J. P. & Velden, C. S. 2004, *Bulletin of the American Meteorological Society*, 85, 353
- Fried, D. L. 1965, *J. Opt. Soc. Am.*, 55, 1427
- Henriques, V. M. J. 2012, *A&A*, 548, A114, <http://arxiv.org/abs/1210.4168>
- Kentischer, T. J., Schmidt, W., Sigwarth, M., & Uexkuell, M. V. 1998, *A&A*, 340, 569

- Landsman, W. B. 1993, in *Astronomical Society of the Pacific Conference Series*, Vol. 52, *Astronomical Data Analysis Software and Systems II*, ed. R. J. Hanisch, R. J. V. Brissenden, & J. Barnes, 246, see also <http://idlastro.gsfc.nasa.gov>
- Leenaarts, J., de la Cruz Rodríguez, J., Kochukhov, O., & Carlsson, M. 2014, *ApJ*, 784, L17
- Löfdahl, M. G. 2002, in *Proc. SPIE*, Vol. 4792, *Image Reconstruction from Incomplete Data II*, ed. P. J. Bones, M. A. Fiddy, & R. P. Millane, 146–155
- Löfdahl, M. G., Henriques, V. M. J., & Kiselman, D. 2011, *A&A*, 533, A82
- Löfdahl, M. G. & Scharmer, G. B. 2012, *A&A*, 537, A80
- Markwardt, C. B. 2009, in *ASP Conf. Ser.*, Vol. 411, *Astronomical Data Analysis Software and Systems XVIII*, ed. D. A. Bohlender, D. Durand, & P. Dowler, 251
- Norén, A. 2013, Bachelor's thesis, Stockholm University, <http://arxiv.org/abs/1311.5148>
- Reardon, K. P., Rimmele, T., Tritschler, A., et al. 2009, in *ASP Conf. Ser.*, Vol. 415, *The Second Hinode Science Meeting: Beyond Discovery-Toward Understanding*, ed. B. Lites, M. Cheung, T. Magara, J. Mariska, & K. Reeves, 332
- Roddier, F. 1999, in *Adaptive Optics in Astronomy*, ed. F. Roddier (Cambridge, UK: Cambridge university press), 25–56
- Roddier, N. 1990, *Opt. Eng.*, 29, 1174
- Roupe van der Voort, L. & de la Cruz Rodríguez, J. 2013, *ApJ*, 776, 56
- Scharmer, G. B. 2006, *A&A*, 447, 1111
- Scharmer, G. B., Bjelksjö, K., Korhonen, T. K., Lindberg, B., & Pettersson, B. 2003a, in *Proc. SPIE*, Vol. 4853, *Innovative Telescopes and Instrumentation for Solar Astrophysics*, ed. S. Keil & S. Avakyan, 341–350
- Scharmer, G. B., de la Cruz Rodríguez, J., Sütterlin, P., & Henriques, V. M. J. 2013, *A&A*, 553, A63
- Scharmer, G. B., Dettori, P., Löfdahl, M. G., & Shand, M. 2003b, in *Proc. SPIE*, Vol. 4853, *Innovative Telescopes and Instrumentation for Solar Astrophysics*, ed. S. Keil & S. Avakyan, 370–380
- Scharmer, G. B., Löfdahl, M. G., van Werkhoven, T. I. M., & de la Cruz Rodríguez, J. 2010, *A&A*, 521, A68
- Scharmer, G. B., Narayan, G., Hillberg, T., et al. 2008, *ApJ*, 689, L69
- Scharmer, G. B. & van Werkhoven, T. I. M. 2010, *A&A*, 513, A25, <http://arxiv.org/abs/1002.3151>
- Schnerr, R. S., de La Cruz Rodríguez, J., & van Noort, M. 2011, *A&A*, 534, A45
- Schou, J. 2013, *Private communication*
- Schou, J., Scherrer, P. H., Bush, R. I., et al. 2012, *Sol. Phys.*, 275, 229
- Sekse, D. H., Roupe van der Voort, L., De Pontieu, B., & Scullion, E. 2013, *ApJ*, 769, 44
- Selbing, J. 2005, Master's thesis, Stockholm University, <http://arxiv.org/abs/1010.4142>
- Shine, R. A., Title, A. M., Tarbell, T. D., et al. 1994, *ApJ*, 430, 413
- Stevens, E. G. & Lavine, J. P. 1994, *IEEE transactions on electronic devices*, 41, 1753
- van Noort, M., Roupe van der Voort, L., & Löfdahl, M. G. 2005, *Sol. Phys.*, 228, 191
- van Noort, M. J. & Roupe van der Voort, L. H. M. 2008, *A&A*, 489, 429
- Vissers, G. & Roupe van der Voort, L. 2012, *ApJ*, 750, 22
- Vissers, G. J. M., Roupe van der Voort, L. H. M., & Rutten, R. J. 2013, *ApJ*, 774, 32
- Watanabe, H., Bellot Rubio, L. R., de la Cruz Rodríguez, J., & Roupe van der Voort, L. 2012, *ApJ*, 757, 49
- Wedemeyer, S., Scullion, E., Roupe van der Voort, L., Bosnjak, A., & Antolin, P. 2013, *ApJ*, 774, 123